RSC Advances

ROYAL SOCIETY OF CHEMISTRY

PAPER

View Article Online
View Journal | View Issue

Check for updates

Cite this: *RSC Adv.*, 2026, **16**, 4473

Selective detection of Cu^{2+} in aqueous medium using an acid hydrazide-based chemosensor: experimental and DFT/TDDFT studies

Joardar Gim,[a] Zannatul Kowser, *[a] Dipa Debnath,[a] Redika Sarmin Prieety,[a]
Miss. Tasnim Jahan,[a] Paul G. Waddell, [b] Most Tahera Khatun,[a]
Sahara Khatun Munni,[a] Md. Rashed Khan[a] and Rashedul Islam[a]

Received 19th August 2025
Accepted 11th January 2026

DOI: 10.1039/d5ra06131h

rsc.li/rsc-advances

An acid hydrazide-based Schiff base, *N*'-(4-hydroxybenzylidene)picolinohydrazide (**HP**), was designed and synthesized in a single-step process for the selective detection of Cu^{2+} ions. The structure of **HP** was thoroughly characterized by FTIR, ^{1}H NMR, ^{13}C NMR, HRMS, SCXRD and elemental analysis. The cation-sensing performance of **HP** was investigated using UV-Vis spectroscopy, revealing a rapid response with high selectivity and sensitivity toward Cu^{2+} in MeOH/H_2O (6 : 4, v/v) with a 10 mM HEPES buffer at pH 7.4, with a detection limit of 8.94 μM. Job's plot analysis confirmed a 1 : 1 binding stoichiometry, with an association constant of 4.26×10^{4} M^{-1}. FESEM analysis showed distinct morphological changes upon Cu^{2+} coordination. The SCXRD result exhibits good agreement with DFT and TD-DFT of the probe **HP**. The hole–electron analysis clearly reveals locally excited (LE) characteristics for the free ligand and intramolecular charge transfer (ICT) behavior for the **HP**–Cu^{2+} complex. Furthermore, the **HP** probe demonstrated practical applicability for Cu^{2+} detection in real water samples.

1. Introduction

Ions of transition metals are crucial for human health and provide significant functions in diverse industries, such as medications, diagnostics, and catalysis.[1] It has been proven that abnormalities in the amounts of specific metal ions may perturb normal biological activities.[2] Copper is an essential micronutrient necessary for the growth and development of humans, animals, and plants. It is the third most prevalent trace element in the Earth's crust, behind iron and zinc.[3] A component of almost every human tissue, copper has a role in many physiological functions, such as cellular metabolism, oxidative stress tolerance, and immunological response.[4–6] Copper(II) ions (Cu^{2+}) function as vital cofactors for numerous metalloenzymes, including cytochrome c oxidase, tyrosinase, and superoxide dismutase.[7–9] Dysregulation of copper homeostasis has been associated with various neurodegenerative illnesses, including Alzheimer's dementia, Wilson's disease, Menkes syndrome, and amyotrophic lateral sclerosis (ALS).[10–17] Moreover, copper has significant toxicity to microorganisms including algae, bacteria, viruses, and aquatic creatures.[18] To safeguard human health, the World Health Organization (WHO) has set a maximum permissible level of 31.5 μM for Cu^{2+} in drinking water.[19] The precise detection of copper ions, due to its biological and environmental importance, has garnered significant interest in life and environmental sciences.[20,21] Despite the utilization of various analytical techniques—such as atomic absorption spectroscopy (AAS), anodic stripping voltammetry (ASV), and inductively coupled plasma optical emission spectrometry/mass spectrometry (ICP-OES/MS)—have been employed for copper ion detection,[22–24] their extensive application is constrained by the necessity for costly equipment, skilled operators, and protracted procedures. In contrast, Chemosensors have developed as useful instruments for ion detection, owing to their simplicity, cost-efficiency, and capacity to deliver both qualitative and quantitative data. This allows us to quickly and effectively identify the target ions in a matter of seconds.

In recent years, numerous chemosensors utilizing Schiff bases have been created, as the –C=N framework, when modified with suitable substituents, provides an advantageous platform for the identification of metal ions in aqueous or semi-aqueous environments.[25] The electronic characteristics of Schiff bases can be precisely altered by structural alterations, resulting in unique spectroscopic reactions upon metal binding.

In this study we have synthesized a novel Schiff base receptor, **HP**—an acid hydrazide derivative—via the condensation of 2-pyridinecarboxylic acid hydrazide and 4-

---

[a] *Department of Chemistry, Jashore University of Science and Technology, Jashore-7408, Bangladesh. E-mail: joardargim@gmail.com; zannatulkowser_che@just.edu.bd; debnathdipa018@gmail.com; redikaprity@gmail.com; tasnim.b920@gmail.com; msttaherakhatun92@gmail.com; saharakhatunmunni@gmail.com; rashedkhan039@gmail.com; riju3295@gmail.com*

[b] *Faculty of Science, Agriculture & Engineering, Newcastle University, Newcastle Upon Tyne, NE1 7RU, UK. E-mail: paul.waddell@ncl.ac.uk*

hydroxybenzaldehyde. This receptor has significant sensitivity and selectivity for Cu^{2+} ions in an aqueous environment at pH 7.4. Interaction with Cu^{2+} ions lead **HP** to exhibit notable alterations in its UV-Vis absorbance spectrum, confirming complex formation. The suggested sensing mechanism is also validated by FTIR and DFT analysis. The structure of **HP** has been comprehensively characterized *via* FTIR, ^{1}H NMR, ^{13}C NMR, HRMS, SCXRD and elemental analysis. The probe has also been successfully employed in real sample analysis, underscoring its practical applicability.

2. Experimental

2.1 Materials and methods

All solvents and reagents used throughout the synthesis and spectroscopic analyses were of spectroscopic grade. The primary reagents, 2-pyridinecarboxylic acid hydrazide and 4-hydroxybenzaldehyde, were obtained from TCI (Japan) and utilized with no additional purification upon receipt. Fresh solutions of metal ions were made from their corresponding chloride salts, sourced from Sigma-Aldrich and TCI. FTIR (ATR) spectra were acquired utilizing a PerkinElmer Spectrum 2 spectrometer. The melting points were obtained using a Stuart SMP-30 instrument. ^{1}H and ^{13}C NMR spectra were obtained using Bruker Ascend 600 MHz NMR spectrometer, with chemical shifts (δ) expressed in parts per million (ppm) in relation to internal standards. Electrospray ionization mass spectrometry (ESI-MS) spectra were recorded in positive ion mode on a Thermo Scientific Orbitrap Exploris 120 mass spectrometer. UV-Visible absorption spectra were obtained using HITACHI UH-5300 double-beam spectrophotometer with a 1 cm path length quartz cuvette.

2.2 X-ray data collection and structure determination

Single crystal diffraction data for **HP** were collected at 150 K on a XtaLAB Synergy HyPix-Arc 100 diffractometer using copper radiation ($\lambda_{CuK\alpha} = 1.54184$ Å) equipped with an Oxford Cryosystems CryostreamPlus open-flow N_2 cooling device. Intensities were corrected for absorption using a multifaceted crystal model created by indexing the faces of the crystal for which data were collected.[26] Cell refinement, data collection and data reduction were undertaken *via* the software CrysAlisPro.[27]

The structure was solved using XT[28] and refined by XL[29] using the Olex2 interface.[30] All non-hydrogen atoms were refined anisotropically and hydrogen atoms were positioned with idealised geometry, with the exception of those bound to heteroatoms, the positions of which were located using peaks in the Fourier difference map. The displacement parameters of the hydrogen atoms were constrained using a riding model with $U_{(H)}$ set to be an appropriate multiple of the U_{eq} value of the parent atom. The crystallographic data of **HP** are listed in Table 1.

2.3 Synthesis of probe HP

Scheme 1 illustrates the synthesis of **HP**. A mixture of 2-pyridine carboxylic acid hydrazide (0.567 g, 4.14 mmol) and 4-hydroxybenzaldehyde (0.506 g, 4.14 mmol) in ethanol (20 mL) was stirred for 4 h. A catalytic amount (2–3 drops) of acetic acid

Table 1 Crystallographic data and refinement parameters of the probe **HP**

CCDC 2515488	
Empirical formula	$C_{13}H_{11}N_3O_2$
Formula weight	241.25
Temperature/K	150.0(2)
Crystal system	Orthorhombic
Space group	*Pbca*
a/Å	11.9663(2)
b Å	7.50140(10)
c/Å	25.5657(4)
α/°	90
β/°	90
γ/°	90
Volume/Å^3	2294.88(6)
Z	8
ρ_{calc}g cm^{-3}	1.397
μ/mm^{-1}	0.803
F(000)	1008.0
Crystal size/mm^3	0.18 × 0.06 × 0.05
Radiation	CuKα ($\lambda = 1.54184$)
2Θ range for data collection/°	6.916 to 153.774
Index ranges	$-14 \le h \le 14$, $-6 \le k \le 9$, $-29 \le l \le 30$
Reflections collected	11 496
Independent reflections	2268 [$R_{int} = 0.0226$, $R_{sigma} = 0.0182$]
Data/restraints/parameters	2268/0/169
Goodness-of-fit on F^2	1.060
Final R indexes [$I >= 2\sigma(I)$]	$R_1 = 0.0313$, $wR_2 = 0.0832$
Final R indexes [all data]	$R_1 = 0.0344$, $wR_2 = 0.0858$
Largest diff. Peak/hole/e Å^{-3}	0.16/−0.21

was added into the reaction. After the reaction completed as confirmed by TLC, the precipitate was filtered and washed with cold ethanol to give *N'*-(4-hydroxy benzylidene)picolinohydrazide. Crystals suitable for X-ray diffraction analysis were grown from the slow evaporation of a methanolic solution at room temperature. Yield: 76% mp: 223 °C. FT-IR (ATR, cm^{-1}): 3237 (OH), 3198 (N–H), 1633 (C═O), 1603 (C═N). ^1H NMR (600 MHz, DMSO-d_6, ppm): δ 11.942 (1H, s, NH), 9.976 (1H, s, OH), 8.689–8.682 (1H, d, $J = 4.2$, H–Ar), 8.539 (1H, s, C═NH), 8.123–8.110 (1H, d, $J = 7.8$, H–Ar), 8.046–8.021 (1H, m, H–Ar), 7.652–7.629 (1H, m, H–Ar), 7.567–7.553(1H, d, $J = 8.4$, H–Ar), 6.856–6.842 (1H, d, $J = 8.4$, H–Ar). ^{13}C NMR (150 MHz, CD_3OD, ppm): δ 116.67, 123.77, 126.80, 128.11, 130.81, 138.92, 149.87, 150.56, 151.97, 161.47, 163.0. Elem. anal. cald. for **HP** (%): C, 64.72; H, 4.60; N, 17.42. Found: C, 61.94; H, 4.43; N, 16.16. HRMS-ESI(*m*/*z*) calcd for $C_{13}H_{11}N_3O_2$ $[M + H]^+$242.0927, found 242.0922.

2.4 Procedure of measurement

The addition of methanol as a co-solvent was needed as probe **HP** is not wholly soluble in 100% aqueous medium. By dissolving the required amount, a stock solution of **HP** at a concentration of 1 mM was prepared. In tests, the solution of **HP** was further diluted to a suitable concentration (10 μM) with a mixed solution of $MeOH/H_2O$ (6 : 4 v/v, HEPES = 10 mM, pH 7.4), and other metal ion solutions (1 mM) (*e.g.*, Na^+, Ni^{2+}, NH_4^+, K^+, Cu^{2+}, Fe^{3+}, Cr^{3+}, Al^{3+}, Sn^{2+}, Cd^{2+}, Zn^{2+}, Pb^{2+}, Ag^+) were made in the same solvent system. Then, in aqueous solvent medium $MeOH/H_2O$ (6 : 4 v/v, HEPES = 10 mM, pH 7.4), the UV-Vis spectra were recorded. Throughout the whole experiment, Millipore Milli-Q water was used. All UV-Vis studies were conducted at ambient temperature.

3. Results and discussion

3.1 Synthesis and characterization

The chemosensor **HP** was synthesized *via* a condensation reaction between 2-pyridine carboxylic acid hydrazide and 4-hydroxybenzaldehyde in good yield, as shown in Scheme 1. Sensor **HP** was fully characterized by various techniques such as FTIR, ^1H NMR, ^{13}C NMR, HRMS, SCXRD and elemental analysis. The results are well consistent with the expected chemical structure. The FTIR, ^1H NMR, ^{13}C NMR and HRMS spectra were shown in Fig. S1–S4 of the SI.

3.2 UV-Vis spectral studies

Probe **HP** (10 μM) in $MeOH/H_2O$ (6 : 4 v/v, HEPES = 10 mM, pH 7.4) exhibited a clear absorption band at 323 nm with a shoulder peak at 223 nm in its UV-Vis absorption spectra (Fig. 1), the band at 323 nm was ascribed to $n \rightarrow \pi^*$ transitions, whereas the band at 223 nm was designated for $\pi \rightarrow \pi^*$ transitions. To examine the selective sensing capabilities of probe **HP** (10 μM) towards various metal ions (1 mM) of environmental and biological relevance, including Na^+, Ni^{2+}, NH_4^+, K^+, Cu^{2+}, Fe^{3+}, Cr^{3+}, Al^{3+}, Sn^{2+}, Cd^{2+}, Zn^{2+}, Hg^{2+}, Pb^{2+} and Ag^+ these ions were introduced into a solution of **HP** in $MeOH/H_2O$ (6 : 4 v/v, HEPES = 10 mM, pH 7.4). No notable spectrum alterations of probe **HP** were observed, with the exception of Cu^{2+}. After the addition of Cu^{2+} to the solution of probe the absorption band of **HP** at 323 nm totally diminished, while a new band emerged at 280 nm. The results indicate that **HP** exhibits high sensitivity and selectivity for Cu^{2+} in a $MeOH/H_2O$ (6 : 4 v/v, HEPES = 10 mM, pH 7.4).

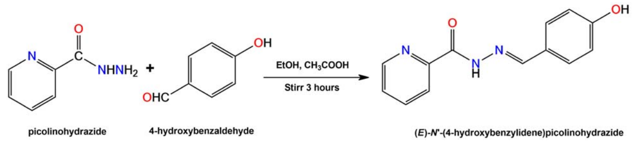

Scheme 1 Synthesis of receptor **HP**.

3.3 Interference of other metal ions

The interference test was conducted to assess the practical application of probe **HP**, as illustrated in Fig. 2. The competition experiments were performed by monitoring the absorbance variations before and after the addition of Cu^{2+} (1×10^{-3} M) to the **HP** solution containing various metal ion interferents ($MeOH/H_2O$ = 6 : 4 v/v, HEPES = 10 mM, pH 7.4) at 280 nm. The ligand, **HP** treated with Cu^{2+} in the presence of various mono- and divalent ions (Na^+, Ni^{2+}, NH_4^+, K^+, Fe^{3+}, Cr^{3+}, Al^{3+}, Sn^{2+}, Cd^{2+}, Zn^{2+}, Hg^{2+}, Pb^{2+}, and Ag^+, each at 1×10^{-3} M) showed no significant spectral changes. These results indicate that the presence of other metal ions did not interfere with the detection of Cu^{2+} by the probe **HP**, as shown in Fig. 2. Furthermore, the interference study **HP** (10 μM) + Cu^{2+} (1×10^{-3} M) was extended to a wider concentration range of competing metal ions (up to 1×10^{-1} M), and even at this elevated concentration, no noticeable interference with the **HP**–Cu^{2+} signal was observed (Fig. S6).

3.4 UV-Vis spectral titration and stoichiometry studies

To better understand the sensing ability of probe **HP**, we performed UV-Vis titrations of probe **HP** through the incremental addition of varying quantities of Cu^{2+} ions (0.1 to 12 equivalents) in a $MeOH/H_2O$ (6 : 4 v/v) solution containing 10 mM HEPES at pH 7.4. In a 10 μM solution of **HP**, the titration graph shows a peak at 223 nm after the addition of 0.1 to 0.5

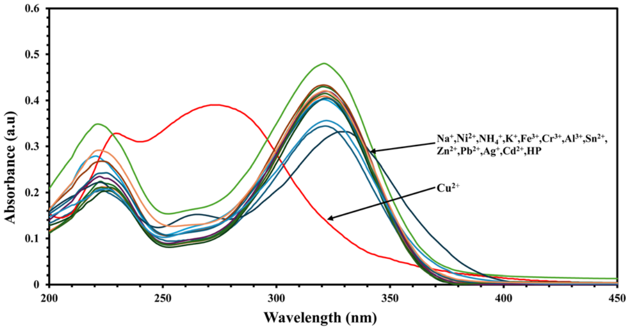

Fig. 1 UV-Vis absorption changes of probe **HP** (10 μM) in $MeOH/H_2O$ (6 : 4 v/v, HEPES = 10 mM, pH 7.4) in the presence of various metal ions.

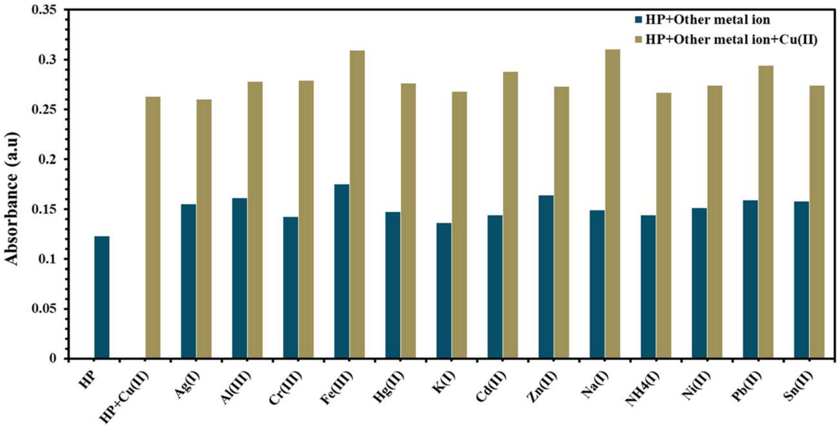

Fig. 2 UV-Vis absorption responses of probe **HP** (10 μM) in the presence of dual metal ions (Cu^{2+} and other specified metal ions, each at 1×10^{-3} M) in $MeOH/H_2O$ (6 : 4 v/v, HEPES = 10 mM, pH 7.4).

equivalents of Cu^{2+}, which shifts to 230 nm for 1 to 12 equivalents of Cu^{2+}. To gain a better understanding of the sensing ability of probe **HP**, UV-Vis titrations were performed by the incremental addition of varying concentrations of Cu^{2+} ions (0.1–12 equivalents) to a $MeOH/H_2O$ (6 : 4, v/v) solution containing 10 mM HEPES at pH 7.4. In a 10 μM solution of **HP**, the titration spectrum exhibited a peak at 223 nm upon the addition of 0.1–0.5 equivalents of Cu^{2+}, which shifted to 230 nm with the addition of 1–12 equivalents of Cu^{2+}. Simultaneously, the absorption band of **HP** at 323 nm was diminished after the addition of 0.1–0.5 equivalents of Cu^{2+} and new absorption bands were appeared at 280 nm for 0.1–12 equivalents of Cu^{2+}, indicating the formation of the **HP**–Cu^{2+} complex.

(Fig. 3). The stoichiometry of binding between **HP** and Cu^{2+} was found using the Job's plot approach, revealing a maximum absorbance at 0.5, as illustrated in Fig. 4. This particular point suggests that the stoichiometry of the binding between probe **HP** and Cu^{2+} is 1 : 1.

The limit of detection of probe **HP** was determined using the equation: detection limit = $3\sigma/m$, where σ is the standard deviation of the blank solution, and m is the slope of the absorbance *versus* [Cu^{2+}] calibration curve.[31,32] The detection limits of **HP** toward Cu^{2+} ion is 8.94 μM (Fig. S5), this is much below the maximum allowable level of 31.5 μM for Cu^{2+} in

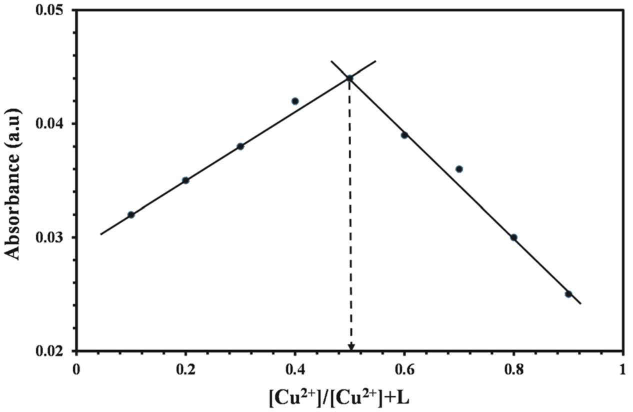

Fig. 4 Job's Plot showing 1 : 1 binding stoichiometry between **HP** and Cu^{2+} in $MeOH/H_2O$ (6 : 4 v/v, HEPES = 10 mM, pH 7.4).

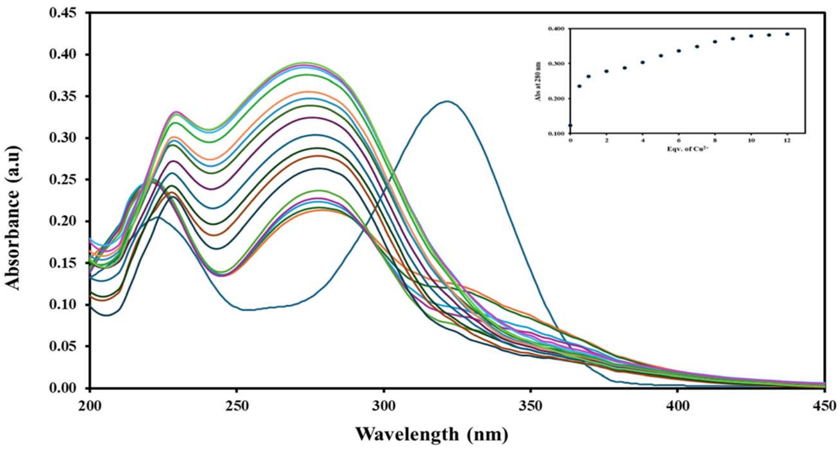

Fig. 3 UV-Vis absorption spectrum of probe **HP** (10 μM) in $MeOH/H_2O$ (6 : 4 v/v, HEPES = 10 mM, pH 7.4) with different concentrations (0.1–12 equiv.) of Cu^{2+}.

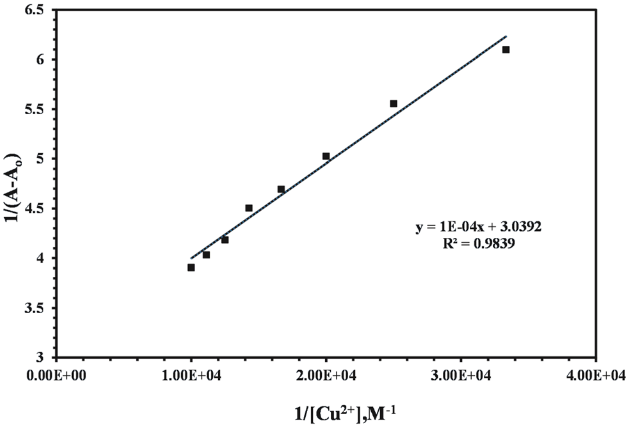

Fig. 5 Benesi–Hildebrand plot (absorbance at 270 nm) of probe HP considering 1 : 1 binding stoichiometry with Cu^{2+}.

drinking water as per World Health Organization standards (1993).[19,33] Additionally, the Benesi–Hildebrand method was employed to ascertain the binding constant for **HP** and Cu^{2+} and was found to be 3.04×10^4 M^{-1}.[34–36] The 1 : 1 binding stoichiometry of the **HP**–Cu^{2+} complex was further confirmed by the linear relationship between $1/A - A_0$ and $1/[Cu^{2+}]$ (Fig. 5).

3.5 Microscopic studies

Furthermore, for a better understanding of the variations in surface topography, field emission scanning electron microscopy (FESEM) of **HP** and **HP**–Cu^{2+} were analyzed, as illustrated in Fig. 6a and b. FESEM photos reveal variations before and after complexation, displaying a highly crystalline morphology characterized by unique rod- or needle-like structures in probe **HP**. These elongated blocks exhibit smooth surfaces and sharp edges, indicating well-ordered molecular packing in the solid state. The morphology undergoes a significant transformation upon complexation with Cu^{2+}. The formerly organized rod-shaped crystals are no longer discernible.

The chemical compositions of **HP** and **HP**–Cu^{2+} were determined using Energy Dispersive X-ray analysis (EDAX) (Fig. 6c and d), which directly confirms the presence of carbon (C), oxygen (O), nitrogen (N), and copper (Cu) components in the produced **HP** and **HP**–Cu^{2+} complex.

3.6 FT-IR analysis

FT-IR spectroscopy was utilized to elucidate the coordination mechanism and structural alterations throughout complexation. Characteristic vibrational bands of the free probe **HP** were identified at 3238 cm^{-1} (O–H stretching), 3201 cm^{-1} (N–H stretching), 1633 cm^{-1} (C=O stretching), and 1603 cm^{-1} (C=N stretching). Substantial spectrum alterations were found upon coordination with Cu^{2+} ions. The O–H and N–H stretching bands converged into a single broad absorption, indicating strong participation of these groups in coordination. The C=N stretching band changed marginally from 1603 to 1598 cm^{-1}, indicating a contact between the imine nitrogen and the Cu^{2+}. Conversely, the C=O stretching band remained fixed at 1633 cm^{-1}, revealing no participation of the carbonyl group in metal coordination. These observations clearly corroborate the coordination of Cu^{2+} with the hydroxyl, amino, and imine nitrogen of probe **HP** (Fig. 7). The suggested binding mechanism is shown in Scheme 2, based on the aforementioned data.

3.7 X-ray crystal structure and DFT-optimized structures

The main crystal parameters are reported in Table 1. The ORTEP and DFT-optimized diagrams of **HP** structures and their corresponding parameters are illustrated in Fig. 8. $C_{13}H_{11}N_3O_2$

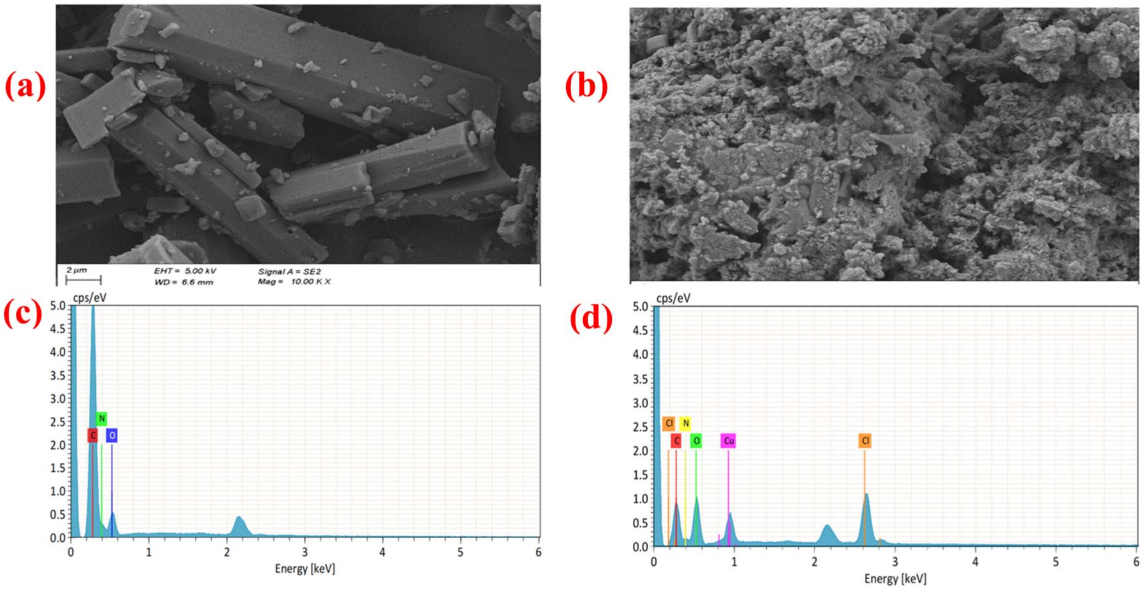

Fig. 6 Alterations in surface topography in FESEM images of (a) probe HP, (b) probe HP–Cu^{2+}, and EDAX analysis of (c) probe HP and (d) probe HP–Cu^{2+}.

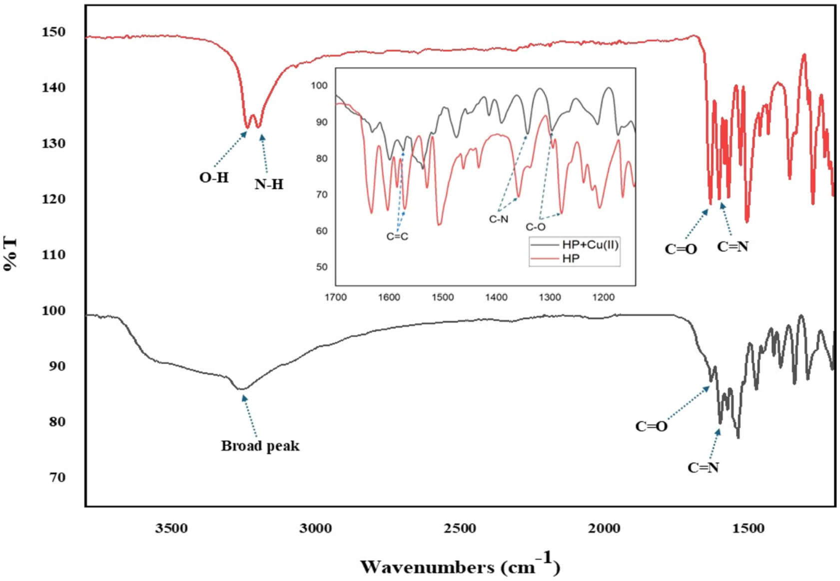

Fig. 7 FT-IR spectra of (a) probe **HP** (red) (b) probe **HP**–Cu^{2+}(black). (Lower wavenumbers peak are at the inset).

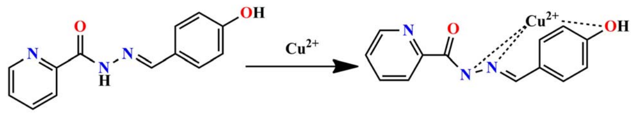

Scheme 2 Proposed binding mechanism.

is orthorhombic in the crystal system. The XRD-parameters of the **HP** ligand structure, like bond distances and the values of their angles, were matched with those derived from the computed DFT/B3LYP/6-311++G(d,p) calculation. An excellent match between calculated and measured results was illustrated, as can be seen in Fig. 9. The correlation between the experimental and calculated bond distances is 0.9718 (Fig. 9a and b). Similarly, the correlation between the calculated and experimental angles is 0.9608 (Fig. 9c and d). The DFT-optimized and ORTEP bond length and angles values have been reported in Tables S1 and S2.

3.8 Frontier molecular orbital analysis

To elucidate the electronic structure, electron density distribution, kinetic stability, and reactivity of the sensor and its complex, Frontier Molecular Orbital Analysis was performed on isolated molecules. The HOMO is generally linked to electron-donating ability, whereas the LUMO is regarded as possessing electron-accepting aptitude. The HOMO and LUMO band gaps are crucial characteristics that influence the electronic behavior of molecules. The presence of positive frequencies for all the structures ensures minimum in the potential energy surface. The optimized geometries of **HP** and **HP**–Cu^{2+} complexes at the B3LYP/6-311++G(d,p) and LANL2DZ level of theory are shown in Fig. 10.

Fig. 11 depicts the frontier molecular orbital (FMO) energies of the probe **HP** and it's complex. The computed HOMO and LUMO values for the free receptor **HP** are −6.37 eV and −1.70 eV, respectively, resulting in an energy gap of 4.67 eV. The coordination of Cu^{2+} with **HP** results in a reduction of the energy gap to 3.26 eV. Using the B3LYP/6-311++G(d,p) level of theory, the calculated FT-IR spectra of **HP** and its Cu^{2+} complex are displayed in Fig. 12. For receptor **HP**, four distinct absorption bands are observed at 1647, 1757, 3488, and 3831 cm^{-1}, corresponding to the C=N, C=O, N–H, and O–H vibrations, respectively. Upon complexation with Cu^{2+}, significant shifts in these vibrational bands are noted at 1654, 1577, 3412, and 3647 cm^{-1}, respectively. These changes indicate strong interactions between the metal ion and the donor sites of the ligand.

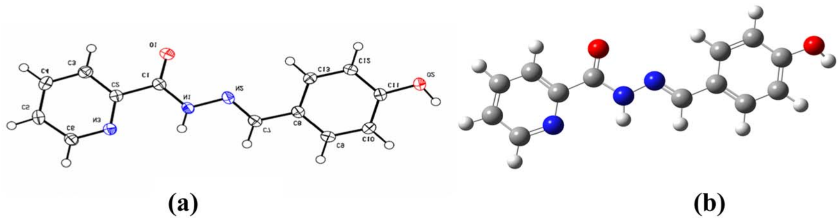
(a) (b)

Fig. 8 Ligand structure: (a) ORTEP diagram (50% probability) and (b) optimized ground state geometries at B3LYP/6-31G++(d,p).

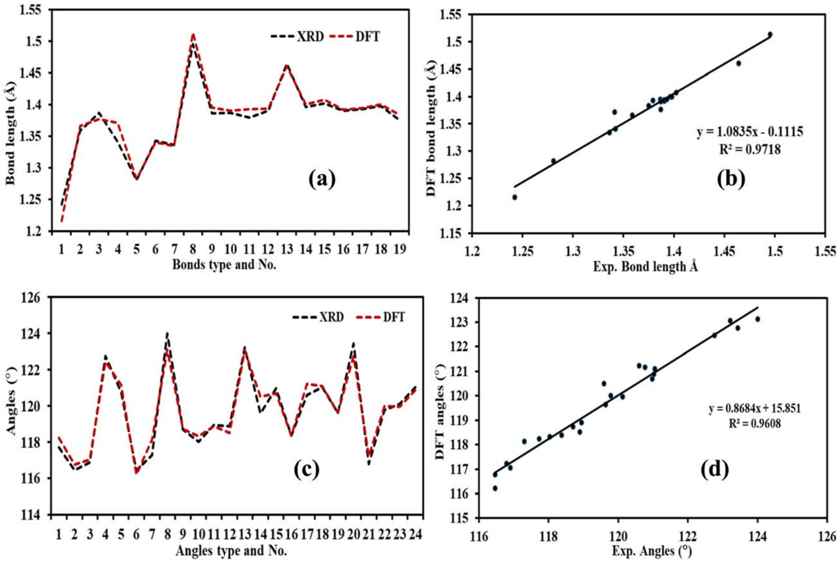

Fig. 9 (a) XRD/DFT-bond lengths histogram, (b) XRD/DFT-bond lengths graphical correlation, (c) XRD/DFT-angles histogram, and (d) DFT/Exp. angles correlation diagram.

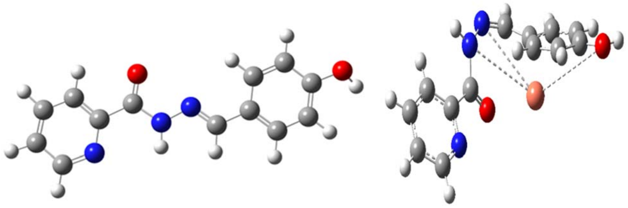

Fig. 10 Optimized structure of **HP** (left) and the **HP**–Cu^{2+} complex (right), calculated by DFT.

Fig. 13 illustrates the graphical depiction of Mulliken atomic charges for the structures. The Mulliken data indicate that all hydrogen atoms possess positive charges, while the majority of carbon atoms exhibit negative charges.

3.8.1 TD-DFT analysis. Time-dependent density functional theory (TD-DFT) computations were carried out in order to investigate the UV-Visible absorption properties of the free ligand **HP** and its Copper(II) complex (**HP**–Cu^{2+}). The computations employed the B3LYP functional, along with the 6-311++G(d,p) basis set for non-metal atoms and the LANL2DZ basis set for the Cu^{2+} ion. To account for solvent effects, the conductor-like polarizable continuum model (CPCM) was employed using methanol as the solvent. The simulated spectra are depicted in Fig. 14, with specific excitation parameters listed in Table 2. The unbound **HP** molecule has exhibited a pronounced absorption maximum at 292.21 nm, which corresponds to an excitation energy of 4.24 eV and an oscillator strength of $f = 0.33$, located in the ultraviolet spectrum. Furthermore, two other transitions are noted at 281.90 nm (4.40 eV, $f = 0.162$) and 275.40 nm (4.50 eV, $f = 0.0248$). The spectrum experiences a notable red shift upon coordination with Cu^{2+}. The first absorption band for the **HP**–Cu^{2+} compound appears at 2389.34 nm (0.518 eV, $f = 0.0048$), signifying a transition into the near-infrared spectrum. Two further absorptions are observed at 1262.17 nm (0.982 eV, $f = 0.0196$) and 943.62 nm (1.31 eV, $f = 0.1052$), indicating significant modifications in the electronic structure following complexation. Fig. 14 illustrates the comparison of TD-DFT spectra for the ligand and its metal complex, confirming the alterations in electronic transitions induced by the metal.

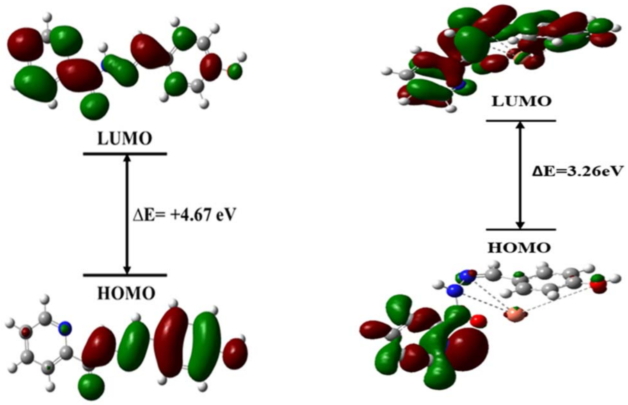

Fig. 11 Frontier molecular orbitals of **HP** (left) and **HP**–Cu^{2+}(right) complex.

3.8.2 Hole–electron analysis. Electron–hole analysis facilitates an intuitive and statistical comprehension of the dynamics and distribution of electrons and holes within a molecule. This enables the discernment of excitation kinds, including local excitation (LE), charge transfer (CT), or Rydberg excitation, predicated on the spatial attributes of the electron and hole distributions. A charge transfer (CT) state is characterized by considerable spatial separation between the hole and electron, often situated in distinct areas of the molecule, in contrast to local excitation where they predominantly overlap. To

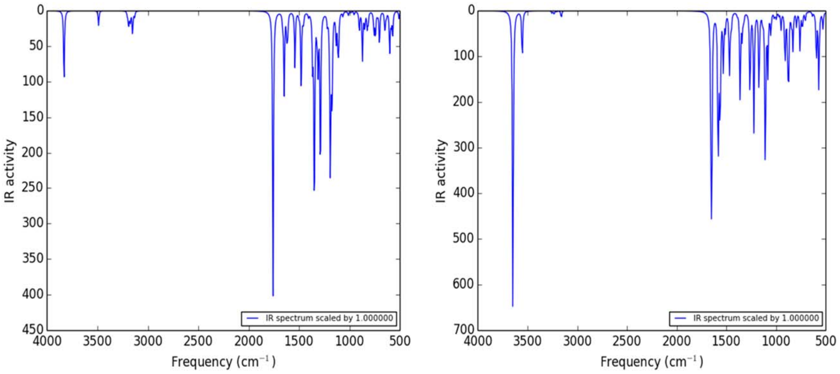

Fig. 12 FT-IR spectra of **HP** (left) and **HP**–Cu^{2+}(right) complex calculated at the B3LYP/6-311++G(d,p) level of theory.

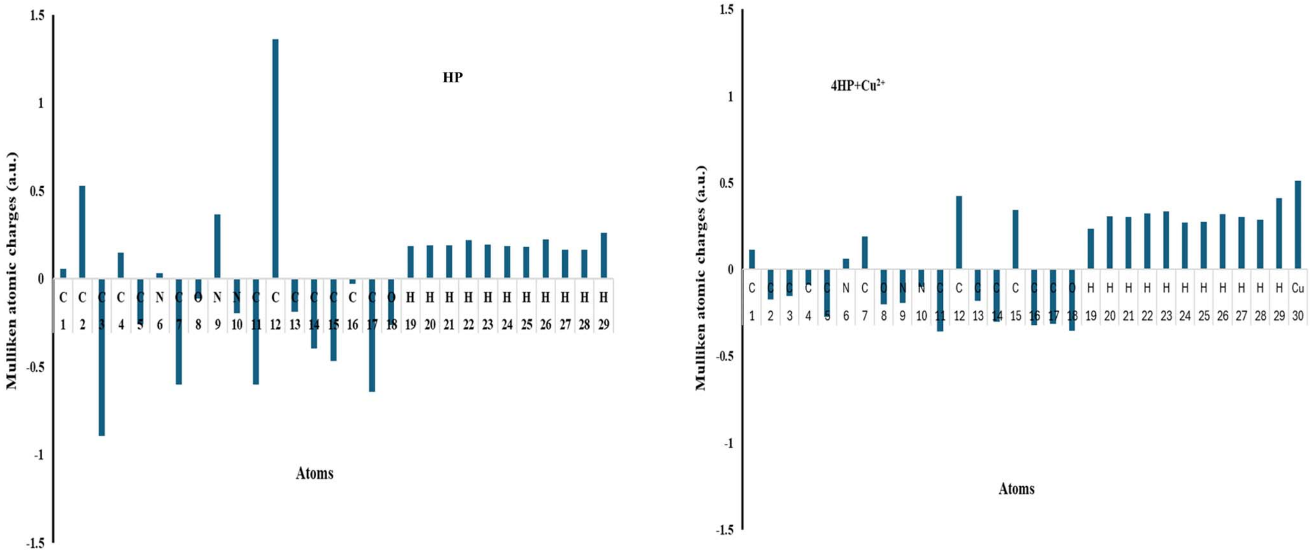

Fig. 13 Mulliken atomic charges of **HP** and **HP**–Cu^{2+} obtained at the B3LYP/6 311++G(d,p) level of theory.

investigate the characteristics of the initial singlet excited state (S_1), we conducted hole–electron analysis utilizing the Multiwfn program. Fig. 15 illustrates the spatial distributions of the hole (blue isosurface) and electron (green isosurface) for the free ligand (**HP**) and its Cu^{2+} complex (**HP**–Cu^{2+}). In the free ligand, the hole density is primarily localized on the imine and phenolic aromatic rings, while the electron density is more diffusely distributed across the adjacent π-conjugated framework. Upon coordination with Cu^{2+}, the hole density shifts toward the donor atoms (N and O) and the picolinohydrazide moiety, whereas the electron density becomes predominantly delocalized over the phenolic moiety and donor atoms

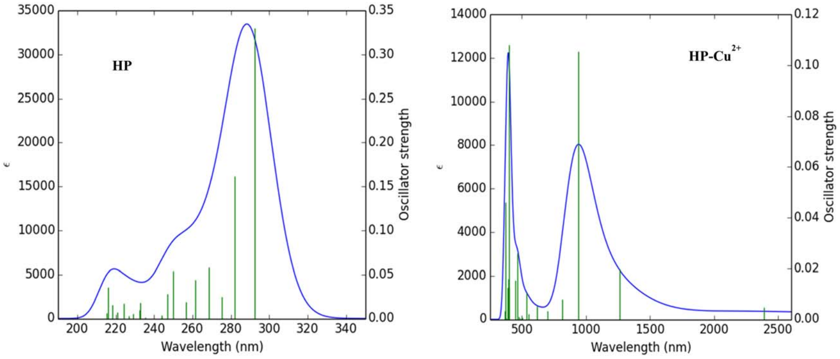

Fig. 14 TD DFT UV-Vis absorption spectra of the probe **HP** and complex **HP**-Cu^{2+}.

Table 2 Calculated transition energies (eV), maximum absorption wavelengths (λ_{max}), oscillator strengths (f_{os}), and major molecular orbital (MO) contributions for the HP and HP–Cu^{2+} complex

Compound	λ (nm)	E (eV)	f_{os}	MO contributions (major contribution, <30%)
HP	292.21	4.24	0.33	HOMO > LUMO (78%)
	281.90	4.40	0.162	H − 1 > LUMO (44%)
	275.40	4.50	0.0248	HOMO > L + 1(38%), HOMO > L + 2 (42%)
HP–Cu^{2+}	2389.34	0.518	0.0048	HOMO(B) > LUMO(B) (98%)
	1262.17	0.982	0.0196	H − 2(B) > LUMO(B) (36%), H − 1(B) > LUMO(B) (60%)
	943.62	1.31	0.1052	H − 2(B) > LUMO(B) (58%), H − 1(B) > LUMO(B) (36%)

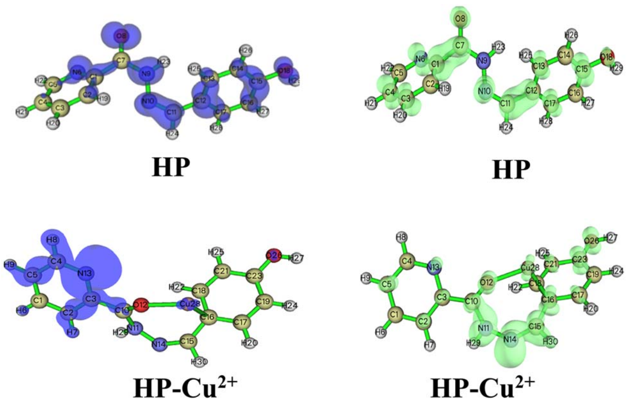

Fig. 15 Plot of hole (blue) and electron (green) distributions of HP and its complex HP–Cu^{2+}.

indicating a coordination-induced reorganization of the electronic distribution.

Table 3 summarizes the quantitative descriptors derived from Multiwfn analysis, which include Sr (spatial overlap integral), D (centroid distance between hole and electron), H (combined spatial extent of hole and electron), t (separation threshold), $\Delta\sigma$ (difference in spatial spread), HDI (hole delocalization index), and EDI (electron delocalization index).

These metrics jointly facilitate the classification of electronic excitation characteristics. Characteristic intramolecular charge transfer (ICT) typically correlates with low Sr values (<0.6), substantial D values (>4.0 Å), and prominent H (>6.5 Å) or t (>0.3 Å) values, indicating considerable spatial separation. Conversely, local excitation (LE) transitions are generally characterized by elevated Sr (>0.6) and diminished D and H values, signifying localized excitation. Our work reveals that the $S_0 \rightarrow S_1$ transition of the free ligand (**HP**) exhibits characteristic LE behavior, with Sr = 0.64, D = 1.039 Å, H = 3.371 Å, and t = −1.717 Å. The Cu^{2+} combination (**HP**–Cu^{2+}) exhibits distinct ICT properties, indicated by Sr = 0.32, D = 3.892 Å, H = 2.434 Å, and t = 2.188 Å. These data validate a shift from a locally excited state in the unbound ligand to a charge transfer state following coordination with Cu^{2+}.

Table 3 Electron–hole analysis descriptors for HP and its Cu^{2+} complex (HP–Cu^{2+})

Descriptor	**HP**	**HP**–Cu^{2+} complex
Excitation	$S_0 \rightarrow S_1$	$S_0 \rightarrow S_1$
E (eV)	4.241	0.519
Sr index (a.u.)	0.64146	0.32662
D index (Å)	1.039	3.892
H Index (Å)	3.371	2.434
t index (Å)	−1.717	2.188
HDI	8.61	20.20
EDI	6.68	10.52
E_{Coul} (eV)	4.152	3.686

3.8.3 NBO analysis. NBO studies were employed to analyze the intramolecular charge transfer between the occupied donor and the empty acceptor orbitals.[37] The delocalization of electron density between Lewis-type Natural Bond Orbitals (NBO), including donor, bonding, or lone-pair orbitals, and non-Lewis-type NBO, such as acceptor or anti-bonding orbitals, serves as the stabilizing force in the donor–acceptor system.[38,39] The second-order Fock matrix has been included to evaluate the interactions between the donor and the acceptor.

The stability of the complex was assessed by NBO analysis by analyzing electron transfer from bonding and lone pair orbitals to antibonding orbitals (Table 4). The most significant intramolecular charge transfer (ICT) was found for the π(C19–C23) → LP*(σ) C23 interaction, with a stabilization energy of 26.51 kcal mol^{-1}. Notable $\pi \rightarrow \pi^*$ interactions comprise π(C16–C17) → π^*(N14–C15) at 20.63 kcal mol^{-1}, and π(C2–C3) → π^*(C10–O12) with a stabilization energy of 17.00 kcal mol^{-1}. The lone pair orbital LP(σ) on C19 significantly donates to the π^*(C16–C17) acceptor, exhibiting a substantial stabilization energy of 75.68 kcal mol^{-1}, which signifies considerable electron delocalization.

Additional significant interactions comprise LP(σ) C5 → π^*(C4–N13) at 15.50 kcal mol^{-1} and LP(σ) N11 → π^*(C10–O12) at 21.70 kcal mol^{-1}, hence affirming the participation of heteroatoms in electron donation. The σ(C15–H30) → σ^*(N11–N14) interaction provides a moderate stabilization energy of 5.59 kcal mol^{-1}, indicative of hyperconjugation effects.

Metal coordination was validated by the donation of LP(O12) to LP*(Cu28), with energies of 10.01 and 8.71 kcal mol^{-1} for the two lone pair orbitals on oxygen engaging with the copper antibonding orbitals, indicating coordination bonding. Additional LP(π) interactions, such as LP(O26) → LP*(C23) (36.79 kcal mol^{-1}), substantially enhance the overall stability.

The donor–acceptor interactions collectively indicate that electron delocalization *via* π and σ bonding frameworks, facilitated by lone pair electron donation and metal coordination, plays an important role for stabilizing the complex.

Table 4 Natural bond orbital analysis for HP–Cu^{2+}

No.	Donor NBO(i)	Acceptor NBO (j)	$E(2)$ kcal mol^{-1}[a]	$E(j) - E(i)$ a.u[b]	$F(i,j)$ a.u[c]
1	BD (π) C2–C3	LP* (σ) C1	20.96	0.18	0.090
2	BD (π) C2–C3	BD* (π) C10–O12	17.00	0.20	0.074
3	BD (π) C4–N13	LP (σ) C5	15.50	0.18	0.082
4	BD (π) C4–N13	BD* (π) C2–C3	12.21	0.29	0.078
5	BD (σ) C15–H30	BD* (σ) N11–N14	5.59	0.86	0.088
6	BD (π) C16–C17	BD* (π) N14–C15	20.63	0.24	0.090
7	BD (π) C16–C17	BD* (π) C18–C21	9.68	0.32	0.073
8	BD (π) C18–C21	LP* (σ) C23	26.51	0.13	0.090
9	BD (π) C18–C21	BD* (π) C16–C17	7.17	0.25	0.057
10	LP* (σ) C1	BD* (π) C2–C3	45.09	0.10	0.108
11	LP (σ) C5	BD* (π) C4–N13	40.29	0.12	0.111
12	LP (σ) N11	BD* (π) C10–O12	21.70	0.30	0.104
13	LP (σ) N11	BD* (π) N14–C15	7.34	0.29	0.059
14	LP (π) O12	BD* (σ) C3–C10	7.28	0.82	0.099
15	LP (π) O12	BD* (σ) C10–N11	7.35	0.67	0.089
16	LP (σ) N13	BD* (σ) C2–C3	5.80	0.82	0.088
17	LP (σ) N13	BD* (σ) C4–C5	5.09	0.84	0.083
18	LP (σ) C19	BD* (π) C16–C17	75.68	0.10	0.124
19	LP* (σ) C23	BD* (π) C18–C21	20.87	0.16	0.099
20	LP (π) O26	LP* (σ) C23	36.79	0.18	0.127
21	BD* (π) C10–O12	BD* (π) C2–C3	16.06	0.08	0.074
22	BD* (π) N14–C15	BD* (π) C16–C17	33.83	0.04	0.069
23	BD* (π) C16–C17	BD* (π) C18–C21	23.31	0.05	0.070
24	LP (σ) O12	LP* (d) Cu28	10.01	0.76	0.111
25	LP (π) O12	LP* (d) Cu28	8.71	0.48	0.083

[a] $E(2)$ means energy of hyperconjugative interactions (stabilization energy). [b] Energy difference between donor and acceptor i and j NBO orbitals. [c] $F(i, j)$ is the Fock matrix element between i and j NBO orbitals.

3.8.4 Adsorption energies of HP with different metal ions. Density Functional Theory simulations were employed to ascertain the adsorption energies. The adsorption energy (Fig. 16) indicated that our ligand (**HP**) exhibited the greatest binding affinity for Cu^{2+} ions.

3.9 Application of chemosensor HP in real samples

Laboratory tap water samples were used to assess the practical usability of the **HP** probe for Cu^{2+} detection. The innate Cu^{2+} concentration in tap water was below the method's assessing limit; therefore, artificial Cu^{2+}-contaminated tap water samples were made by spiking with known amounts of 10 μM and 20 μM of standard Cu^{2+} solutions. The spiked samples were subsequently evaluated using the same exact UV-Vis spectroscopic technique. The concentrations of Cu^{2+} were determined using the calibration curve (absorbance *versus* concentration) depicted in Fig. S5. The recovery values achieved varied from 94.10% to 96.43% (Table 5), demonstrating the method's high accuracy. The results indicate that **HP** demonstrates significant potential for the quantitative detection of Cu^{2+} ions in actual water samples, confirming its relevance in environmental monitoring.

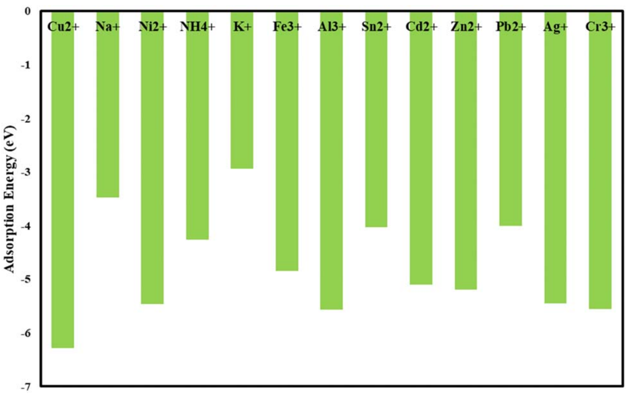

Fig. 16 Adsorption energies of various metal ions with the probe HP.

3.10 Comparison of HP with other Schiff base chemosensors

The efficacy of the Schiff base probe **HP** in detecting Cu^{2+} was evaluated in comparison to several other stated Schiff base chemosensors, as detailed in Table 6. Table 6 illustrates that the present system exhibits several advantageous analytical features compared to other systems, including high sensitivity, high selectivity, a lower detection limit, straightforward operational technology, good solubility, and practical applicability. The synthesis of the proposed chemosensor **HP** involves a single

Table 5 Real water sample analysis of HP for the Cu^{2+} ion

Metal ion	Spiked amount (μM)	Recovered amount (μM)	Recovery %
Cu^{2+}	10	9.41	94.10
	20	19.28	96.43

Table 6 Comparison of **HP** with other reported Schiff base chemosensors

Probe	Solvent	LOD	Binding constant	M : L ratio	Ref.
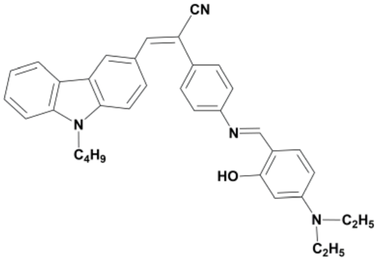	CH_3CN-Tris (20 mM, v/v = 1 : 1, pH = 7.2)	11.4 μM	1.47×10^5 M^{-1}	1 : 1	40
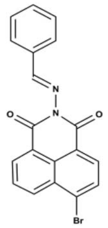	CH_3CN	12.5 μM	Not reported	1 : 1	31
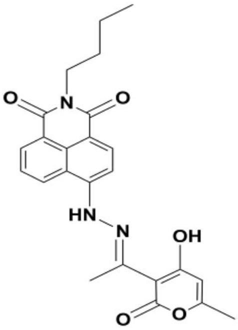	THF/H_2O	15.14 μM	1.26×10^5 M^{-1}	1 : 2	41
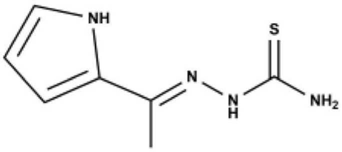	(DMSO/TrisHCl),1 : 1,v/v, buffer pH 7	19.7 μM	Not reported	1 : 1	42
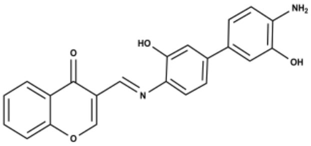	20% H_2O/DMF	15 μM	2.42×10^8 M^{-2}	2 : 1	43
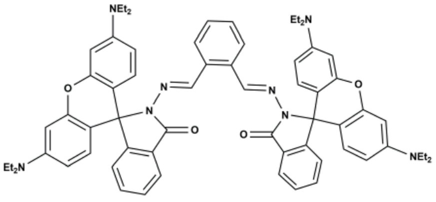	75%CH_3CN 25% 0.01 M Tris–HCl buffer pH 7	69 μM	1.65×10^3 M^{-1}	1 : 1	44
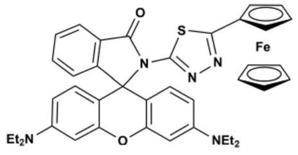	EtOH/HEPES (8 : 2, v/v, pH 7.2)	650 μM	1.73×10^4 M^{-1}	1 : 1	45

Table 6 (*Contd.*)

Probe	Solvent	LOD	Binding constant	M : L ratio	Ref.
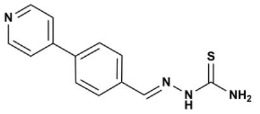	MeOH/H_2O (1 : 1, v/v)	10.67 µM	2.69×10^4 M^{-1}	2 : 1	46
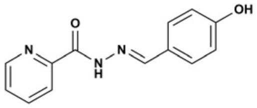	MeOH/H_2O (6 : 4 v/v, HEPES = 10 mM, pH 7.4)	8.94 µM	3.04×10^4 M^{-1}	1 : 1	This work

step, utilizes less hazardous reagents, and does not produce any hazardous by-products.

4. Conclusion

In summary, the compound **HP** was synthesized *via* a simple and efficient one-step methodology and characterized using FTIR, ^{1}H NMR, ^{13}C NMR, HRMS, SCXRD, and elemental analysis. **HP** functions as a chemodosimeter for Cu^{2+} ions, exhibiting distinct absorption changes in MeOH/H_2O (6 : 4, v/v, HEPES = 10 mM, pH 7.4). Job's plot analysis indicated a 1 : 1 binding stoichiometry, while FTIR studies confirmed the complexation process with Cu^{2+} ions. FESEM imaging of the free ligand and its Cu^{2+} complex revealed pronounced morphological changes, further supporting successful coordination. The experimental findings are in excellent agreement with DFT and TD-DFT calculations. NBO analysis validated the stability of the **HP**–Cu^{2+} complex. The hole–electron analysis clearly reveals locally excited (LE) characteristics for the free ligand and intramolecular charge transfer (ICT) behavior for the **HP**–Cu^{2+} complex. The combination of cost-effective and readily available precursors, a high binding constant, and a lower limit of detection (LOD) compared to many reported Cu^{2+} chemosensors positions **HP** as a promising candidate for Cu^{2+} ion detection. Its practical applicability was demonstrated by the high sensitivity achieved in detecting trace concentrations of Cu^{2+} in real water samples.

Author contributions statement

Joardar Gim: Performed the experiment and all computational studies, analyzed and interpreted the data, wrote the paper. Zannatul Kowser: conceptualized the whole experiment, supervised students, contributed materials, reagents, analysis tools, or data, analyzed and interpreted the data, wrote the paper, and revised the manuscript. Dipa Debnath: performed the experimental part. Redika Sarmin Prieety: performed the experimental part. Miss. Tasnim Jahan: performed the experimental part. Paul G. Waddell: single-crystal X-ray diffraction data collection, structure solution and refinement, crystallographic interpretation, manuscript writing, and critical revision. Most Tahera Khatun: performed the experimental part. Sahara Khatun Munni: performed the experimental part. Md. Rashed Khan: wrote the paper. Rashedul Islam: revised the manuscript.

Conflicts of interest

The authors declare that they have no conflict of interest.

Data availability

CCDC 2515488 contains the supplementary crystallographic data for this paper.[47]

Supplementary information (SI) is available. See DOI: https://doi.org/10.1039/d5ra06131h.

Acknowledgements

Zannatul Kowser is thankful to Jashore University of Science and Technology Research Cell (JUSTRC), Jashore 7408, Bangladesh, under grant number 24-FoS-08 for the fiscal year 2024 to 2025 for providing financial support to carry out a part of the study. The authors gratefully acknowledge the Department of Chemistry, of Jashore University of Science and Technology (JUST) for providing data analysis support.

References

1 A. Taha, N. Farooq, N. Singh and A. A. Hashmi, *J. Mol. Liq.*, 2024, **401**, 124678.
2 S.-H. Park, N. Kwon, J.-H. Lee, J. Yoon and I. Shin, *Chem. Soc. Rev.*, 2020, **49**, 143–179.
3 M. Prajapati, N. Pandey, S. Kalla, S. Bandaru and A. Sivaiah, *Sens. Diagn.*, 2024, **3**, 412–420.
4 M. Valko, K. Jomova, C. J. Rhodes, K. Kuča and K. Musílek, *Arch. Toxicol.*, 2016, **90**, 1–37.
5 L. Banci, I. Bertini, S. Ciofi-Baffoni, T. Kozyreva, K. Zovo and P. Palumaa, *Nature*, 2010, **465**, 645–648.
6 P. Matak, S. Zumerle, M. Mastrogiannaki, S. El Balkhi, S. Delga, J. R. R. Mathieu, F. Canonne-Hergaux, J. Poupon,

P. A. Sharp, S. Vaulont and C. Peyssonnaux, *PLoS One*, 2013, **8**, e59538.

7 I. A. Koval, P. Gamez, C. Belle, K. Selmeczi and J. Reedijk, *Chem. Soc. Rev.*, 2006, **35**, 814.

8 E. L. Que, D. W. Domaille and C. J. Chang, *Chem. Rev.*, 2008, **108**, 1517–1549.

9 S. Poormoradkhan Melal, B. Khalili, N. O. Mahmoodi and M. Pasandideh Nadamani, *J Photochem Photobiol A Chem*, 2025, **460**, 116140.

10 Z. K. Mathys and A. R. White, *Adv. Neurobiol.*, 2017, **18**, 199–216.

11 A. Lucena-Valera, P. Ruz-Zafra and J. Ampuero, *Med. Clin.*, 2023, **160**, 261–267.

12 J. Chen, Y. Jiang, H. Shi, Y. Peng, X. Fan and C. Li, *Pflugers Arch*, 2020, **472**, 1415–1429.

13 Q. Y. Chen, P. Wu, T. Wen, X. Qin, R. Zhang, R. Jia, J. Jin, F. Hu, X. Xie and J. Dang, *Front. Aging Neurosci.*, 2022, **17**(14), 970711.

14 L. McAlary, V. K. Shephard, G. S. A. Wright and J. J. Yerbury, *J. Biol. Chem.*, 2022, **298**, 101612.

15 G. Mohammadi Ziarani, N. Shamkhali, Z. Panahande, M. Feizi-Dehnayebi and A. Badiei, *Results Chem*, 2025, **16**, 102381.

16 B. Thangaraj, M. Ponram, S. Ranganathan, B. Sambath, R. Cingaram, S. K. Iyer and K. Natesan Sundaramurthy, *RSC Adv.*, 2023, **13**, 26023–26030.

17 P. Deng, Y. Pei, M. Liu, W. Song, M. Wang, F. Wang, C. Wu and L. Xu, *RSC Adv.*, 2021, **11**, 7610–7620.

18 C. Lawrence, G. E. Sanders and C. Wilson, in *Management of Animal Care and Use Programs in Research, Education, and Testing*, CRC Press, 2nd edn, Boca Raton, Taylor & Francis, 2018, pp. 559–578.

19 National Research Council (US) Committee, *Copper in Drinking Water*, National Academies Press (US), Washington (DC), 2000.

20 R. Kumar, B. Singh, P. Gahlyan, A. Verma, M. Bhandari, R. Kakkar and B. Pani, *RSC Adv.*, 2024, **14**, 23083–23094.

21 W.-Y. Zhu, K. Liu and X. Zhang, *Sens. Diagn.*, 2023, **2**, 665–675.

22 J. Pizarro, E. Flores, V. Jimenez, T. Maldonado, C. Saitz, A. Vega, F. Godoy and R. Segura, *Sens Actuators B Chem*, 2019, **281**, 115–122.

23 N. Li, D. Zhang, Q. Zhang, Y. Lu, J. Jiang, G. L. Liu and Q. Liu, *Sens Actuators B Chem*, 2016, **231**, 349–356.

24 L. Lago, O. R. B. Thomas and B. R. Roberts, *J Chromatogr A*, 2020, **1616**, 460806.

25 J. Wang, Y. Gao, Y. Zhang, D. Xu, Z. Li, Y. Su, F. Wang, N. Zhang, D. Zhang, K. Wang and Y. Chen, *New J. Chem.*, 2025, **49**, 9133–9144.

26 R. C. Clark and J. S. Reid, *Acta Crystallogr A*, 1995, **51**, 887–897.

27 *CrysAlisPro*, Rigaku Oxford Diffraction, Tokyo, Japan.

28 G. M. Sheldrick, *Acta Crystallogr., Sect. A:Found. Adv.*, 2015, **71**, 3–8.

29 G. M. Sheldrick, *Acta Crystallogr A*, 2008, **64**, 112–122.

30 O. V. Dolomanov, L. J. Bourhis, R. J. Gildea, J. A. K. Howard and H. Puschmann, *J. Appl. Crystallogr.*, 2009, **42**, 339–341.

31 G. Kaur, G. Kumar and I. Singh, *J. Mol. Struct.*, 2025, **1319**, 139252.

32 P. Seenu and S. K. Iyer, *Sens. Diagn.*, 2025, **4**, 973–983.

33 R. Gajendhiran, A. K. R. Ahmed, S. Mithra, S. A. Majeed, A. S. S. Hameed, S. Jegadeeshwari, K. Muthu, M. NizamMohideen and A. K. Rahiman, *Anal. Methods*, 2025, **17**, 7920–7935.

34 S. Sarkar, A. Chatterjee, K. Ghosh, N. N. Ghosh, A. Dutta, A. Kumar, A. K. Mandal and K. Biswas, *New J. Chem.*, 2025, **49**, 10991–11000.

35 S. Schoeman, N. Mama and L. Myburgh, *New J. Chem.*, 2025, **49**, 1745–1754.

36 B. Zhang, D. Zeng, Y.-X. Zhang, P. Pan, J. Wang, A. Shen, J.-X. Lu, Y.-J. Zhu, A.-P. Xing and J. Yuan, *Spectrochim Acta A Mol Biomol Spectrosc*, 2025, **340**, 126310.

37 T. Saleem, S. Khan, M. Yaqub, M. Khalid, M. Islam, M. Yousaf ur Rehman, M. Rashid, I. Shafiq, A. A. C. Braga, A. Syed, A. H. Bahkali, J. F. Trant and Z. Shafiq, *New J. Chem.*, 2022, **46**, 18233–18243.

38 V. Pophristic, L. Goodman and N. Guchhait, *J. Phys. Chem. A*, 1997, **101**, 4290–4297.

39 F. Weinhold, *Nature*, 2001, **411**, 539–541.

40 X. Liu, P. Xu, X. Zhao, J. Ge, C. Huang, W. Zhu, C. Li, L. Du and M. Fang, *Inorganica Chim Acta*, 2019, **495**, 118975.

41 N. Saini, N. Prigyai, C. Wannasiri, V. Ervithayasuporn and S. Kiatkamjornwong, *J Photochem Photobiol A Chem*, 2018, **358**, 215–225.

42 E. Normaya, N. A. Baharu and M. N. Ahmad, *J. Mol. Struct.*, 2020, **1212**, 128094.

43 A. Dhawale and D. R. Trivedi, *ACS Omega*, 2025, **10**, 9527–9536.

44 A. J. Weerasinghe, F. A. Abebe and E. Sinn, *Tetrahedron Lett.*, 2011, **52**, 5648–5651.

45 H. Ye, F. Ge, X.-C. Chen, Y. Li, H. Zhang, B.-X. Zhao and J.-Y. Miao, *Sens Actuators B Chem*, 2013, **182**, 273–279.

46 A. K. Manna, J. Mondal, R. Chandra, K. Rout and G. K. Patra, *J Photochem Photobiol A Chem*, 2018, **356**, 477–488.

47 CCDC 2515488: Experimental Crystal Structure Determination, 2026, DOI: 10.5517/ccdc.csd.cc2qfksj.